SCIENCE CHINA
Physics, Mechanics & Astronomy

•Article•

May 2023 Vol. 66 No. 5: 256111
https://doi.org/10.1007/s11433-022-2079-1

Influence of thermal history on the crystallization behavior of high-B_s Fe-based amorphous alloys

Bowen Zang[1], Lijian Song[1,2*], Richard Parsons[3], Jie Shen[4], Meng Gao[1], Yan Zhang[1], Juntao Huo[1,2], Yonghao Sun[4], Fushan Li[5], Kiyonori Suzuki[3*], Jun-Qiang Wang[1,2*], and Weihua Wang[4]

[1] *CAS Key Laboratory of Magnetic Materials and Devices, and Zhejiang Province Key Laboratory of Magnetic Materials and Application Technology, Ningbo Institute of Materials Technology and Engineering, Chinese Academy of Sciences, Ningbo 315201, China;*
[2] *Center of Materials Science and Optoelectronics Engineering, University of Chinese Academy of Sciences, Beijing 100049, China;*
[3] *Department of Materials Science and Engineering, Monash University, Clayton VIC 3800, Australia;*
[4] *Institute of Physics, Chinese Academy of Sciences, Beijing 100190, China;*
[5] *School of Materials Science and Engineering, Zhengzhou University, Zhengzhou 450001, China*

Received November 29, 2022; accepted February 13, 2023; published online April 7, 2023

A crucial step in creating cutting-edge soft magnetic alloys is the nanocrystallization of Fe-based amorphous alloys. However, it is unclear how the thermal history affects the nanocrystallization. In this work, high-precision nanocalorimetry and *in-situ* high-temperature transmission electron microscopy are used to systematically examine how the pre-annealing relaxation process affects the nanocrystallization of Fe-based amorphous alloys. We discover that the glass with more thermal energy storage will crystallize into superb nanocrystalline structures with exceptionally advanced soft magnetism. The soft magnetic properties of Fe-B nanocrystalline alloys can be improved by increasing the relaxation temperature. This finding provides solid and clear evidence for the influences of thermal history on crystallization behavior for Fe-based amorphous alloys, which is helpful for designing advanced soft magnetic nanocrystalline alloys.

amorphous alloys, enthalpy relaxation, nanocrystallization, microstructure development, soft magnetic properties

PACS number(s): 61.43.Dq, 75.75.+a, 75.50.Tt, 64.70.Kb

Citation: B. Zang, L. Song, R. Parsons, J. Shen, M. Gao, Y. Zhang, J. Huo, Y. Sun, F. Li, K. Suzuki, J.-Q. Wang, and W. Wang, Influence of thermal history on the crystallization behavior of high-B_s Fe-based amorphous alloys, Sci. China-Phys. Mech. Astron. **66**, 256111 (2023), https://doi.org/10.1007/s11433-022-2079-1

1 Introduction

The invention of exceptional soft magnetic materials is desired by the increasingly electrified world and the growing demands for sustainable development of the society [1]. Due to their exceptional soft magnetic properties that are suitable for contemporary electric and electronic applications, Fe-based amorphous and nanocrystalline alloys have received considerable attention [2-12]. Nanocrystallization is a crucial step to produce soft magnets with higher saturation magnetic induction (B_s) and lower core loss than the Fe-based amorphous alloys [6,9,13]. The good magnetic softness of the nanocrystallized alloys is directly related to the microstructure [14-16]. Nanocrystallized alloys provide the probability to achieve both high B_s and good magnetic softness

*Corresponding authors (Lijian Song, email: songlj@nimte.ac.cn; Kiyonori Suzuki, email: kiyonori.suzuki@monash.edu; Jun-Qiang Wang, email: jqwang@nimte.ac.cn)

(i.e., low coercivity and low core loss). The high-B_s Fe-based nanocrystalline alloys with a B_s of 1.75-2.0 T and a core loss only 10%-25% of that of Si-steel have been developed in the previous decade [2,3,7,8,17-19].

Due to the high viscosity, homogeneous nucleation of nanocrystals is kinetically unfavored in amorphous alloys [20-23]. Diffusion-controlled growth of the heterogeneously nucleated grains dominates the crystallization in high-*B* Fe-based amorphous alloys, which usually have a number density (N) of about 10^{18}-10^{22} m^{-3} (depends on the quenching process) [4,20,24-27]. In earlier studies, the goal was to produce a monolithic glass precursor with a high number density of heterogeneous nucleation sites and a slowed growth kinetics [28-30]. It has recently garnered a lot of interest to generate high number density (~10^{23} m^{-3}) of pre-crystallites in the as-quenched amorphous precursors by well-matched glass-forming ability and cooling rate [18,31,32]. All these studies rely on changing the composition, particularly the minor-alloying of the non-magnetic element Cu which may create a high number density of nanocrystals ($N \approx 10^{23}$-10^{24} m^{-3}). However, the alloying of non-magnetic elements invariably decreases the B_s. Refining the nanostructure of nanocrystallized alloys by modifying the heat treatment process is favored because it will not decrease the B_s [13,27,33-37]. However, due to the stochastic dynamics of crystallization, precisely managing the nanocrystallization behavior remains quite challenging.

Recent studies found that the crystallization behavior of amorphous systems is strongly influenced by the thermal history above T_g (e.g., in supercooled liquid state) [38-40]. Additionally, the enthalpy relaxation of an Au-based amorphous alloy also significantly affected the crystallization kinetics [41]. Since Fe-based amorphous alloys usually do not show the obvious supercooled liquid region, their thermal history might be memorized in the amorphous state and inherited to the crystallization process. Studying how the thermal history affects the nanocrystallization process in Fe-based amorphous alloys is therefore very interesting. In this study, we investigated the effect of relaxation on the isothermal crystallization behavior using a $Fe_{86}B_{14}$ amorphous alloy with a high-Fe concentration. $Fe_{86}B_{14}$ was chosen as the model substance because it is simple in composition. It is free of the alloying elements that have a strong influence on the crystallization kinetics (e.g., Nb, Ni, Cu, etc.) or on the soft magnetic properties (e.g., Co, Si). A high-precision chip-based differential scanning calorimetry (Flash DSC) that can give a heating rate up to 10^4 K/s was used to evaluate the enthalpy evolution. The outcomes demonstrated that the crystallization kinetics, microstructure, and soft magnetic properties of Fe-based nanocrystalline alloys were directly influenced by the relaxation conditions.

2 Experimental section

2.1 Sample fabrication

$Fe_{86}B_{14}$ ingots were prepared by arc melting 99.98 wt.% pure iron pieces and 99.9 wt.% pure boron pieces in a Ti-gettered Ar atmosphere. $Fe_{86}B_{14}$ ribbons with a thickness of 10-11 μm and a width of 10-12 mm were prepared in an Ar atmosphere by a single roller melt spinner using a copper wheel with a circumferential speed of 50 m/s.

2.2 Nanocalorimetry measurements

Nanocalorimetry experiments were performed by Mettler Toledo Flash DSC which is capable of heating/cooling at rates up to 10^4 K/s. The as-spun ribbons were diced into 100 μm × 100 μm and 20 μm × 20 μm squares by high precision Ni blade for nanocalorimetry tests. Isothermal annealing tests were performed by heating an amorphous sample to the isothermal annealing temperature (T_a) at a fixed heating rate (R_h) and annealing it isothermally. The sample was then cooled down to room temperature at a cooling rate (R_c) of -3×10^3 K/s. More details about the experiment procedures are provided in Supporting Information.

2.3 Crystallization kinetics analysis

The crystallization kinetics of amorphous $Fe_{86}B_{14}$ undergone different thermal histories was analyzed by Komogrov-Johnson-Mehl-Avrami (KJMA) model. The conversion of fractional enthalpy change (dH/dH_{max}) to the volume fraction of phase transformation (f_t) was done by the procedures described in Supporting Information.

2.4 Microstructure characterization

The FDSC samples were cut and thinned by a focused ion beam (FIB, Auriga by Car Zeiss) microscope for transmission electron microscope (TEM) observations. The microstructure of samples was observed by Tecnai Talos F200X TEM and Tecnai F20 TEM operated under 200 kV high-tension. The *in-situ* crystallization experiments were performed by welding the amorphous samples onto a chip and heating the chip by Joule heating in the Talos F200X microscope ($R_h \approx 1000$ K/s). Pre-relaxation of the amorphous samples for the *in-situ* experiment was done by a home-made rapid annealing furnace with an $R_h \approx 5000$ K/s.

2.5 Magnetic properties characterization

Ribbons with a length of 70 mm were fast annealed by a home-made rapid annealing furnace. The peak heating rate was about 5000 K/s to mimic the Flash DSC measurement.

The coercivity of ribbons was measured using a Rikken Denshi DC B-H tracer. The core loss of ribbons was measured by a Rikken Denshi AC B-H analyzer. The relative permeability of ribbons was estimated from the inductance values measured by an impedance analyzer (Agilent 4294A). The saturation magnetic induction values were measured by a vibrating sample magnetometer (VSM, Lakeshore 7410).

3 Results

The as-spun $Fe_{86}B_{14}$ ribbons were amorphous, as confirmed by the X-ray diffraction (XRD) and transmission electron microscopy (TEM) results (see Supporting Information Figure S1). The Flash DSC curves of as-spun $Fe_{86}B_{14}$ (Figure 1(a)) revealed a two-stage phase transformation process, which is typical for this alloy system [24]. A clear glass transition phenomenon was identified at $R_h \geqslant 5000$ K/s, with a glass transition temperature T_g about 800 K. The isothermal annealing temperature (T_a) ranged from 733 to 773 K.

The isothermal heat flow traces of amorphous $Fe_{86}B_{14}$ samples are illustrated in Figure 1(b). Each isothermal heat flow curve has two distinct exothermic peaks. The first exothermic peak is recognized as the relaxation event h_{relax} by performing an isothermal scan twice on the same sample. Detailed information is presented in Figure S2. The second peak is identified as the primary crystallization peak h_x. The labels h_{relax} and h_x refer to the "normalized residual relaxation enthalpy" and the "normalized crystallization enthalpy", respectively.

The Avrami exponent (n) for primary crystallization in amorphous $Fe_{86}B_{14}$ at various T_a are plotted in Figure 1(c). The details on how n was determined are shown in Supporting Information. Under standard annealing conditions, e.g., $R_h \leqslant 1.7$ K/s and $T_a \leqslant 693$ K, the crystallization of $Fe_{86}B_{14}$ amorphous alloys firstly undergoes heterogeneous nucleation and then 3-D grain growth ($n = 1.5$) [26,27]. The fact that n increases from 1.5 to 2.5 suggests that as T_a rises, an extra nucleation mechanism is triggered and even accelerated in the early stage of crystallization ($f_t = 20\%$-40%) (Table S1) [42-44]. The nucleation kinetics are enhanced with a larger value of n, which results in a finer microstructure free of big agglomerates (blue circled) and with a higher number density of grains (Figure 1(d)).

The following experiments were conducted at $T_a = 773$ K, where crystallization involves significant nucleation over

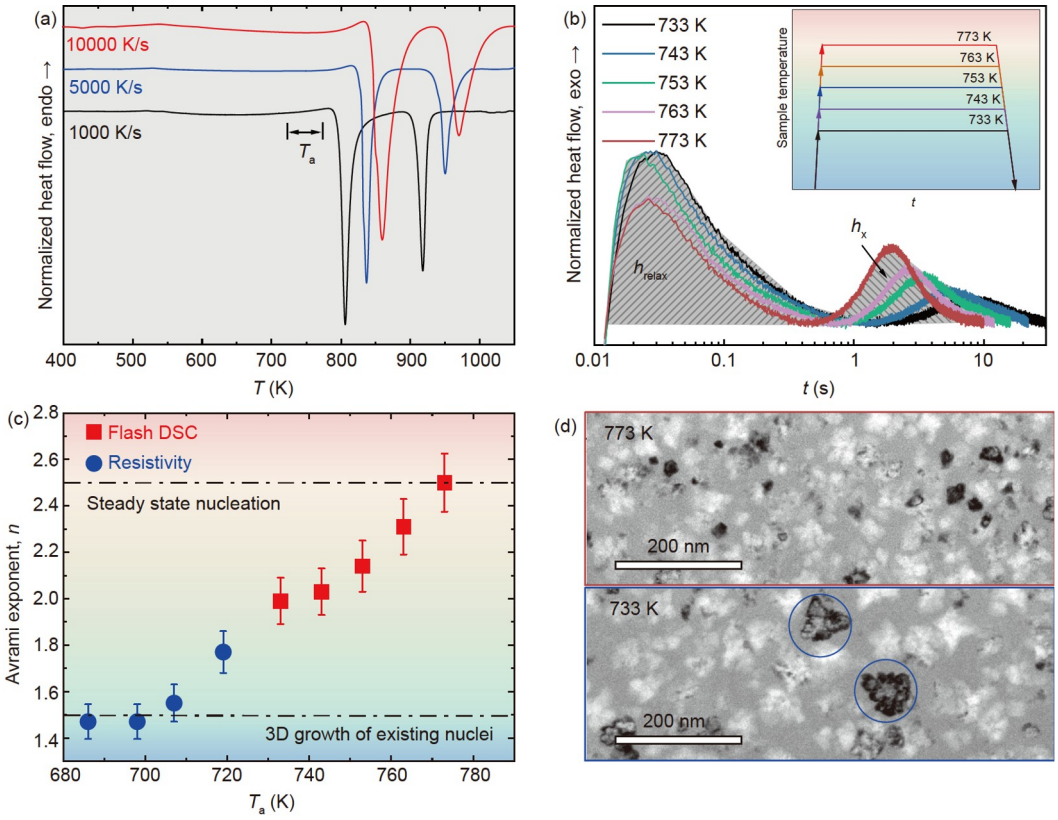

Figure 1 (Color online) (a) Isochronal Flash DSC curves of as-spun $Fe_{86}B_{14}$ at different heating rates (T_{x1} = 795.4, 829.2, 844.2 K for heating rate R_h = 1000, 5000, 10000 K/s, respectively). (b) Isothermal annealing heat flow curves of amorphous $Fe_{86}B_{14}$ at different annealing temperatures (T_a) with R_h = 1000 K/s. The inset shows the annealing protocols. (c) The Avrami exponents (for $f_t = 20\%$-40%) versus T_a plot for the primary crystallization in amorphous $Fe_{86}B_{14}$ [27]. (d) Bright field TEM images of $Fe_{86}B_{14}$ heated at R_h = 1000 K/s and then crystallized isothermally at 733 K ($n = 2.0$, $D = 30.3$ nm) and 773 K ($n = 2.5$, $D = 22.3$ nm) with $f_t = 80\%$-85%.

time ($n \approx 2.5$). To alter the temperature path that the glassy state underwent before crystallization onset, we first varied R_h in a range from 100 to 10000 K/s. For $R_h \geqslant 300$ K/s, the relaxation peak is observable in Figure 2(a). The relaxation state of each sample is represented by the normalized residual relaxation enthalpy, h_{relax}. For $R_h = 10000$ K/s, the h_{relax} reached a maximum whose value was defined as unity; the minimum value of h_{relax} was defined as zero. An unchanging h_x was seen since the entire crystallization process was left to the isothermal stage (Figure 2(b)). Less relaxation enthalpy was consumed on heating as R_h increased, and more relaxation process was reserved to T_a. As a result, the relationship between h_{relax} and R_h is positive (Figure 2(b)). Intriguingly, Figure 2(c) shows a monotonic connection between h_{relax} and the Avrami exponent of primary crystallization in $Fe_{86}B_{14}$. According to this, higher relaxation enthalpy set aside for T_a can facilitate the nucleation kinetics during the early stages of crystallization, which is beneficial for generating a finer and denser nanocrystalline microstructure. Increasing h_{relax} can refine the microstructure and prevent the formation of agglomerates during the nanocrystallization of $Fe_{86}B_{14}$ (blue circled in Figure 2(d)), which is anticipated to achieve superior soft magnetic properties.

On the other hand, by pre-relaxing the amorphous samples at $T_r = 673$ K for various time t_r, the relaxation condition of the glass state may be adjusted (inset of Figure 3(a)). A longer t_r in this protocol triggers more relaxation at 673 K and lowers the h_{relax} at 773 K (Figure 3(a)). The Avrami exponent in Figure 3(b) decreases when t_r is extended, and the sample that has been pre-relaxed at 673 K for 7 s ($h_{relax} \approx 0$) contains more agglomerated grains. Transferring the relaxation process from 673 to 773 K could result in a 10.5% reduction in mean grain size for nanocrystalline $Fe_{86}B_{14}$ (from 24.9 to 22.3 nm). By measuring from the bright field images, the corresponding number density of grains was increased from 1.44×10^{22} to 2.12×10^{22} m^{-3}. The exact values measured by this method are not accurate since the bright field TEM image is only a 2-D projection of a 3-D volume. Since the same standard was used, this measurement could semi-quantitatively reflect the difference in the number density of grains in nanocrystalline $Fe_{86}B_{14}$ with different relaxation conditions prior to crystallization.

To further clarify the effect of relaxation conditions on crystallization, we annealed amorphous $Fe_{86}B_{14}$ with different relaxation conditions *in-situ* in TEM. Figure 4(a) and (f) show the amorphous $Fe_{86}B_{14}$ pre-relaxed at 673 K for 4 s and the as-spun $Fe_{86}B_{14}$, respectively. The samples in Figure 4(a) and (f) were annealed in TEM for 5 s at 773 K, pre-heated at

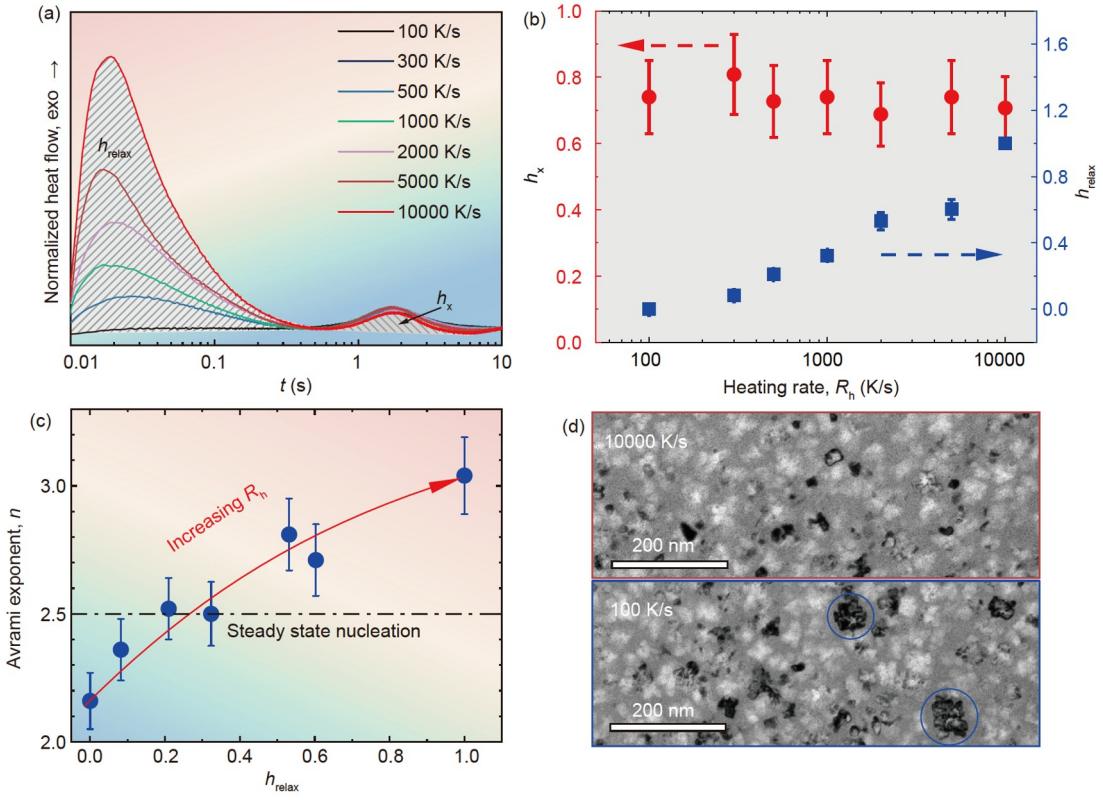

Figure 2 (Color online) (a) Isothermal heat flow curves of as-spun $Fe_{86}B_{14}$ at $T_a = 773$ K with R_h from 100 to 10000 K/s. (b) The normalized crystallization enthalpy (h_x) and normalized residual relaxation enthalpy (h_{relax}) estimated from the isothermal curves in (a). (c) The Avrami exponents (for $f_t = 20\%$-40%) versus h_{relax} plot estimated from the isothermal curves in (a). (d) Bright field TEM images of $Fe_{86}B_{14}$ crystallized isothermally at $T_a = 773$ K with $R_h = 100$ K/s ($n = 2.16$, $D = 24.4$ nm) and $R_h = 10000$ K/s ($n = 3.04$, $D = 20.7$ nm), $f_t = 80\%$-85%.

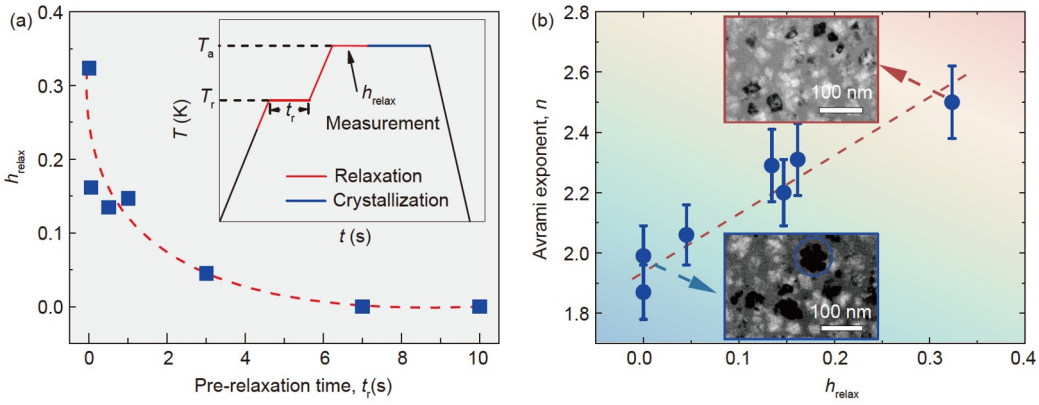

Figure 3 (Color online) (a) The relationship between normalized residual relaxation enthalpy (h_{relax}) at T_a = 773 K and the pre-relaxation time (t_r) at T_r = 673 K. The inset shows the annealing protocol used. (b) The Avrami exponents (for f_t = 20%-40%) versus h_{relax} plot of samples annealed by the annealing protocol in (a) with T_r = 673 K, T_a = 773 K, R_h = 1000 K/s, and t_r from 0 to10 s. The inset shows the microstructure of samples with t_r = 0 (n = 2.5, D = 22.3 nm) and t_r = 7 s (n = 1.99, D = 24.9 nm), f_t = 80%-85%.

R_h = 1000 K/s. *Ex-situ* pre-relaxation at 673 K nearly completed the relaxation for the sample in Figure 4(a). *In-situ* relaxation took place at 773 K for the sample in Figure 4(f) prior to crystallization. Due to the incredibly thin thickness, annealing an amorphous sample in a TEM would accelerate crystallization. The high surface to volume ratio gives the TEM samples plenty of heterogeneous nucleation sites. The sample relaxed at 673 K (Figure 4(d)) exhibits larger grains and more agglomerates than the sample relaxed at 773 K (Figure 4(i)). Figure 4(k) and (l) show the grain size distribution measured from the samples in Figure 4(d) and (i). The grain size in both samples shows a lognormal distribution, lognormal(μ, σ^2). In Figure 4(k), the log-mean of grain size is μ = 2.644 and the log-variance of grain size is σ^2 = 0.408^2. The corresponding arithmetic mean of grain size is 15.4 nm and the standard deviation of grain size is 6.8 nm. In Figure 4(l), the log-mean of grain size is μ = 2.560 and the log-variance of grain size is σ^2 = 0.440^2. The corresponding arithmetic mean of grain size is 14.2 nm and the standard deviation of grain size is 6.4 nm. Raising the relaxation temperature caused an ~8% drop in the arithmetic mean grain size of $Fe_{86}B_{14}$.

The soft magnetic properties of nanocrystalline $Fe_{86}B_{14}$ are directly impacted by the alteration in the crystallization kinetics induced by various relaxation conditions. Using a home-made ultra-rapid annealing (URA) furnace with a peak R_h of up to ~5000 K/s, bulk $Fe_{86}B_{14}$ amorphous ribbons were heated in accordance with the annealing protocols shown in Figure 3(a). $Fe_{86}B_{14}$ has an outstanding B_s of 1.89 T, which is almost the highest among Co-free Fe-based nanocrystalline alloys. By moving the relaxation process from 673 to 773 K, the coercivity of nanocrystalline $Fe_{86}B_{14}$ was reduced by 62%, from 15.5 to 5.9 A/m (Figure 5(a)). Its relative permeability was increased by 105% from 4000 to 8200 (Figure 5(b)). The corresponding core loss value showed a 45% reduction, from 0.42 to 0.23 W/kg (Figure 5(c)). The improvement in soft magnetic properties does not affect the B_s of $Fe_{86}B_{14}$ that remains a super-high level of 1.89 T (Figure 5(d)). Higher enthalpy states of amorphous alloys will yield superior nanocrystalline alloys with enhanced soft magnetism.

4 Discussion

Amorphous precursors of Fe-based nanocrystalline alloys often crystallize before glass transition due to their poor thermal stability. In this case, adding nucleating agents such as Cu appears to be the most effective way to boost the number of bcc-Fe grains, even though doing so degrades the glass-forming ability and B_s. In recent years, increasing the heating rate became another method to improve the soft magnetic properties of Fe-based nanocrystalline alloys [34]. However, the influencing mechanism of heating rate on soft magnetic properties is not clear. Here, our research shows that altering the relaxation conditions of the glassy state can greatly aid in the nucleation of high-B Fe-based nanocrystalline alloy systems.

Figure 6 schematically shows the link between the thermal path and h_{relax} in this work. In the amorphous sample, thermal pathways across the red region yield higher h_{relax}, whereas those through the blue region produce lower h_{relax}. The inset of Figure 6 illustrates how it affects the crystallization of amorphous $Fe_{86}B_{14}$ at 773 K. The nuclei for the samples nanocrystallized through the blue thermal paths have a relatively low number density (e.g., on the magnitude of 10^{22} m^{-3}). On their interface with the amorphous matrix, new grains will be created during crystallization growth. More substantial agglomerates will be present in the resulting nanocrystalline microstructure. On the other hand, an amorphous sample that undergoes the thermal path shown by the red arrows has a mostly restrained relaxation process up to

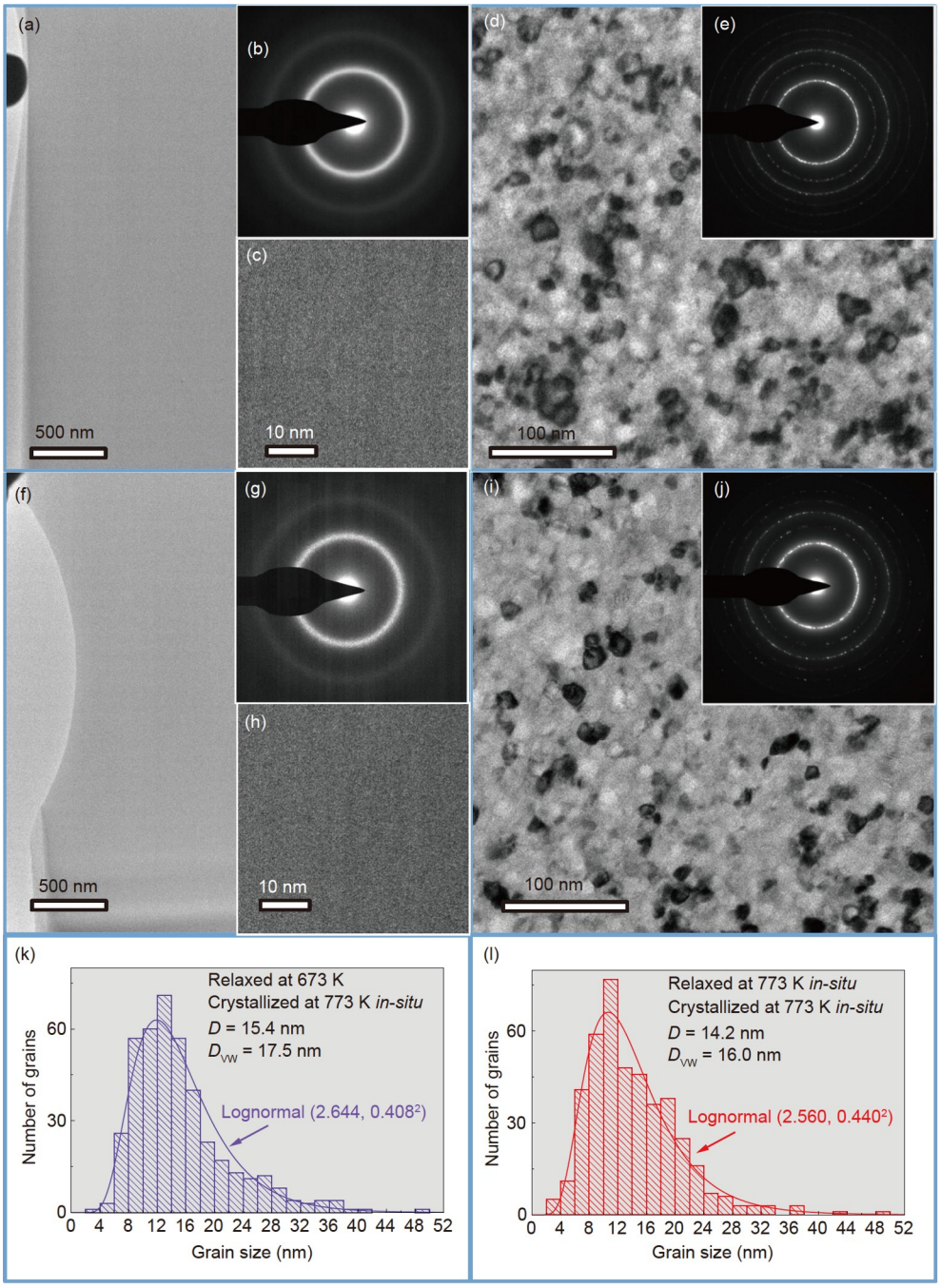

Figure 4 (Color online) (a) Amorphous $Fe_{86}B_{14}$ pre-relaxed at 673 K for 4 s. (b) SAED pattern of the sample in (a). (c) HRTEM image of the sample in (a). (d) Nanocrystalline structure developed *in-situ* from the sample in (a) with T_a = 773 K, t_a = 5 s, R_h = 1000 K/s. (e) SAED pattern of the sample in (d). (f) As-spun $Fe_{86}B_{14}$. (g) SAED pattern of the sample in (f). (h) HRTEM image of the sample in (f). (i) Nanocrystalline structure developed *in-situ* from the sample in (f) with T_a = 773 K, t_a = 5 s, R_h = 1000 K/s. (j) SAED pattern of the sample in (i). (k) Size of bcc-Fe grains (measured from the BF images) in $Fe_{86}B_{14}$ relaxed at 673 K *ex-situ* and then crystallized at 773 K *in-situ*. D represents the arithmetic mean grain size and D_{VW} represents the volume-weighted mean grain size. The size distribution is fitted by lognormal distribution lognormal(μ, σ^2) with the log-mean μ = 2.644 and the log-variance $\sigma^2 = 0.408^2$. (l) Size of bcc-Fe grains (measured from the BF images) in $Fe_{86}B_{14}$ relaxed and crystallized at 773 K *in-situ*. The size distribution is fitted by lognormal distribution with the log-mean μ = 2.560 and the log-variance $\sigma^2 = 0.440^2$.

T_a. Such an amorphous precursor enhances nucleation kinetics, leading to a higher number density (e.g., above 10^{23} m^{-3}) of nuclei during crystallization. Because the grain growth of existing grains is constrained by the promoted formation of fresh crystals, the resulting nanocrystalline microstructure is refined and homogenized.

The clusters in a glass created during cooling may persist in the supercooled liquid state and affect the subsequent crystallization and growth process [38-40]. In addition to the clusters that form during cooling, Song et al. [41] showed

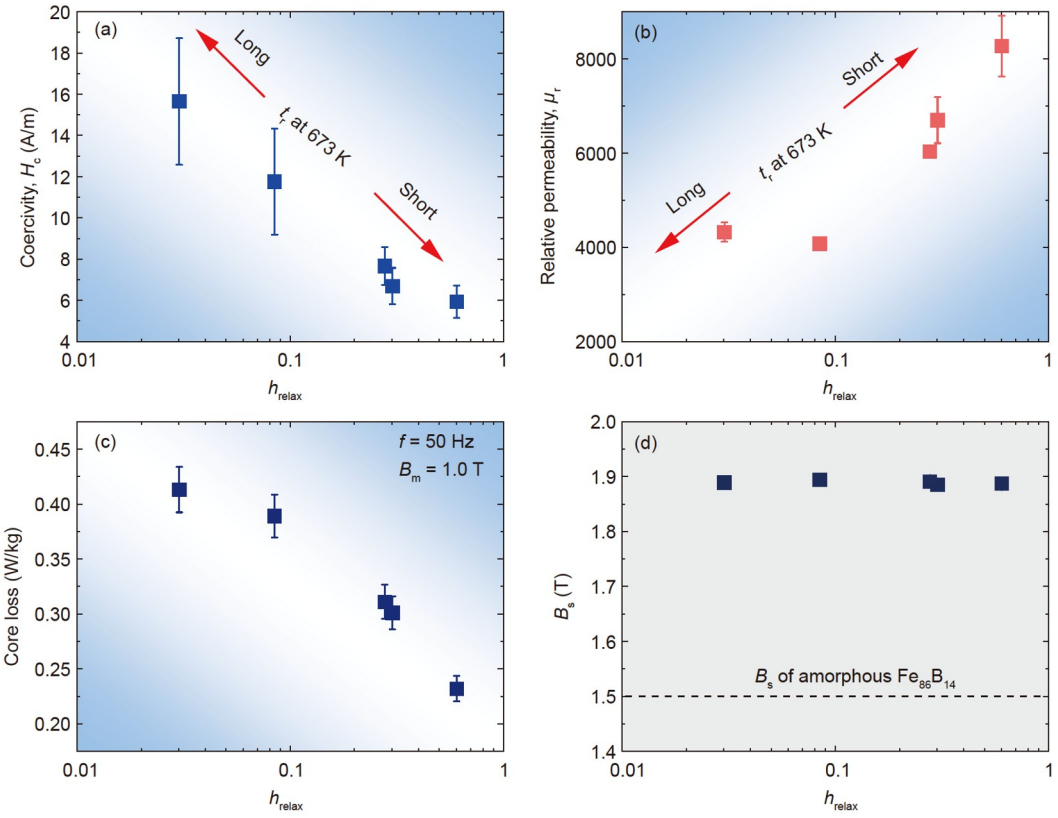

Figure 5 (Color online) Relationship between soft magnetic properties and h_{relax} for nanocrystalline $Fe_{86}B_{14}$ crystallized at 773 K. (a) Coercivity; (b) relative permeability; (c) core loss; (d) saturation magnetic induction.

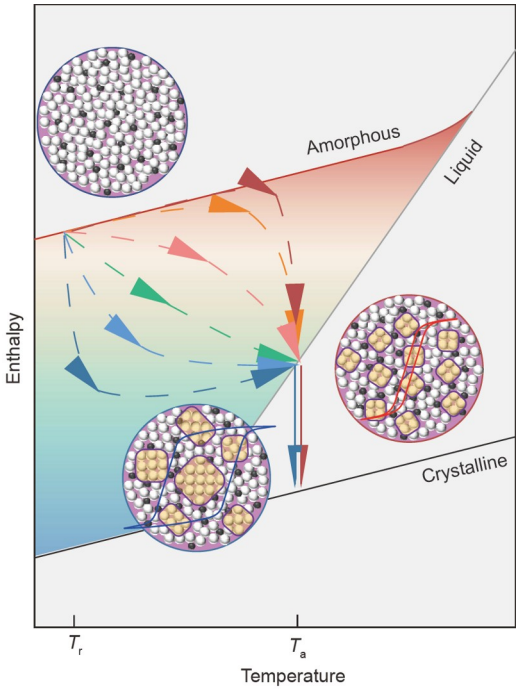

Figure 6 (Color online) Schematic illustration of the thermal history for the glassy state and its influence on the nanocrystallization behavior and magnetic properties. The glass that retains higher energy to higher temperatures will crystallize into finer and more homogeneous nanocrystals that has lower coercivity.

that the microstructural development accumulated during the α relaxation process might also facilitate the crystallization process above T_g. We picked an amorphous alloy system that can crystallize prior to the glass transition. We would assume that the amorphous samples were relaxed to the same enthalpy state before crystallization at a constant T_a because the relaxation peak and the crystallization peak can be clearly identified on each graph. Our results suggest that while the high viscosity of the glassy state restricts atomic mobility throughout the relaxation process, different microstructural features should form and accumulate at various relaxation temperatures. The development of critical nuclei in an amorphous alloy is directly impacted by the microstructural features that emerge below T_g. The development of such microstructural features is thought to be more under control than the cooling-induced cluster formation.

Accelerating the nucleation process is vital for designing advanced soft magnetic nanocrystalline alloys. In the past, the alloying of the element, e.g., Cu, which has positive mixing enthalpy with Fe demonstrated effective to promote the nucleation of Fe nanocrystals [29,45]. However, the alloying of Cu causes some side-effects, e.g., the decrease in glass-forming ability and saturation magnetization [32,34]. Our method proposed in this work derives from the inherent nonequilibrium characteristic of glasses, which should be

universally applicable for different amorphous alloys. Increasing the energy state or retaining the relaxation enthalpy to higher temperatures for amorphous alloys does not need to change their composition and has no influence on glass-forming ability. This makes it a promising and attractive strategy for fabricating advanced nanocrystalline alloys.

5 Conclusion

In summary, a systematic relationship between relaxation conditions and crystallization behavior is established for an amorphous $Fe_{86}B_{14}$ alloy. We find that the crystallization kinetics of amorphous alloys is directly inherited from their relaxation kinetics. For the amorphous $Fe_{86}B_{14}$ alloy, reserving greater relaxation enthalpy at higher temperatures can speed up the nucleation process. An ultra-fine microstructure and good soft magnetic properties are achieved in the high B_s $Fe_{86}B_{14}$ nanocrystalline alloy. These results demonstrate a novel characteristic that is inherited from the glassy state to the crystallization process and will be helpful in the development of advanced soft magnetic nanocrystalline alloys.

This work was supported by the "Pioneer and Leading Goose" R&D Program of Zhejiang (Grant No. 2022C01023), National Natural Science Foundation of China (Grant Nos. 52101205, 92163108, 51922102, 52001319, and 51971239), Hunan Key Laboratory of Design and Manufacture of Electromagnetic Equipment under the Open Foundation (Grant No. DC202005), and Zhejiang Provincial Natural Science Foundation of China (Grant No. LGF22E010002).

Supporting Information

The supporting information is available online at http://phys.scichina.com and https://link.springer.com. The supporting materials are published as submitted, without typesetting or editing. The responsibility for scientific accuracy and content remains entirely with the authors.

1 J. M. Silveyra, E. Ferrara, D. L. Huber, and T. C. Monson, Science **362**, 418 (2018).
2 H. Li, A. Wang, T. Liu, P. Chen, A. He, Q. Li, J. Luan, and C. T. Liu, Mater. Today **42**, 49 (2021).
3 L. Hou, X. Fan, Q. Wang, W. Yang, and B. Shen, J. Mater. Sci. Tech. **35**, 1655 (2019).
4 H. X. Li, Z. C. Lu, S. L. Wang, Y. Wu, and Z. P. Lu, Prog. Mater. Sci. **103**, 235 (2019).
5 E. Lopatina, I. Soldatov, V. Budinsky, M. Marsilius, L. Schultz, G. Herzer, and R. Schäfer, Acta Mater. **96**, 10 (2015).
6 G. Herzer, Acta Mater. **61**, 718 (2013).
7 A. Makino, IEEE Trans. Magn. **48**, 1331 (2012).
8 M. Ohta, and Y. Yoshizawa, Appl. Phys. Lett. **91**, 062517 (2007).
9 K. Suzuki, and G. Herzer, *Advanced Magnetic Nanostructures* (Springer, New York, 2006).
10 Y. Q. Wu, T. Bitoh, K. Hono, A. Makino, and A. Inoue, Acta Mater. **49**, 4069 (2001).
11 K. Suzuki, A. Makino, A. Inoue, and T. Masumoto, J. Appl. Phys. **70**, 6232 (1991).
12 Y. Yoshizawa, S. Oguma, and K. Yamauchi, J. Appl. Phys. **64**, 6044 (1988).
13 K. Suzuki, R. Parsons, B. Zang, K. Onodera, H. Kishimoto, and A. Kato, Appl. Phys. Lett. **110**, 012407 (2017).
14 G. Herzer, IEEE Trans. Magn. **25**, 3327 (1989).
15 G. Herzer, IEEE Trans. Magn. **26**, 1397 (1990).
16 K. Suzuki, and J. M. Cadogan, Phys. Rev. B **58**, 2730 (1998).
17 R. Parsons, B. Zang, K. Onodera, H. Kishimoto, T. Shoji, A. Kato, and K. Suzuki, J. Magn. Magn. Mater. **476**, 142 (2019).
18 X. Jia, B. Zhang, W. Zhang, Y. Dong, J. Li, A. He, and R. W. Li, J. Mater. Sci. Tech. **108**, 186 (2022).
19 Z. Li, R. Parsons, H. Kishimoto, T. Shoji, A. Kato, J. Karel, and K. Suzuki, J. Alloys Compd. **902**, 162544 (2022).
20 A. L. Greer, Acta Metall. **30**, 171 (1982).
21 A. L. Greer, Science **267**, 1947 (1995).
22 V. M. Fokin, E. D. Zanotto, N. S. Yuritsyn, and J. W. P. Schmelzer, J. Non-Cryst. **352**, 2681 (2006).
23 S. Sohn, Y. Jung, Y. Xie, C. Osuji, J. Schroers, and J. J. Cha, Nat. Commun. **6**, 8157 (2015).
24 U. Köster, and U. Herold, *Glassy Metals I* (Springer Verlag, Berlin, 1981).
25 K. Hono, K. Hiraga, Q. Wang, A. Inoue, and T. Sakurai, Acta Metall. Mater. **40**, 2137 (1992).
26 A. Hirata, Y. Hirotsu, E. Matsubara, T. Ohkubo, and K. Hono, Phys. Rev. B **74**, 184204 (2006).
27 B. Zang, R. Parsons, K. Onodera, H. Kishimoto, T. Shoji, A. Kato, J. S. Garitaonandia, A. C. Y. Liu, and K. Suzuki, Phys. Rev. Mater. **4**, 033404 (2020).
28 J. D. Ayers, V. G. Harris, J. A. Sprague, and W. T. Elam, Appl. Phys. Lett. **64**, 974 (1994).
29 J. D. Ayers, V. G. Harris, J. A. Sprague, W. T. Elam, and H. N. Jones, Acta Mater. **46**, 1861 (1998).
30 K. Hono, D. H. Ping, M. Ohnuma, and H. Onodera, Acta Mater. **47**, 997 (1999).
31 M. Nishijima, M. Matsuura, Y. Zhang, and A. Makino, Philos. Mag. Lett. **95**, 277 (2015).
32 Y. Li, X. Jia, W. Zhang, Y. Zhang, G. Xie, Z. Qiu, J. Luan, and Z. Jiao, J. Mater. Sci. Tech. **65**, 171 (2021).
33 K. G. Pradeep, G. Herzer, P. Choi, and D. Raabe, Acta Mater. **68**, 295 (2014).
34 B. Zang, R. Parsons, K. Onodera, H. Kishimoto, A. Kato, A. C. Y. Liu, and K. Suzuki, Scripta Mater. **132**, 68 (2017).
35 R. Parsons, B. Zang, K. Onodera, H. Kishimoto, T. Shoji, A. Kato, and K. Suzuki, J. Phys. D-Appl. Phys. **51**, 415001 (2018).
36 A. Talaat, D. W. Greve, M. V. Suraj, and P. R. Ohodnicki Jr., J. Alloys Compd. **854**, 156480 (2021).
37 R. Parsons, and K. Suzuki, AIP Adv. **12**, 035316 (2022).
38 B. Zhao, B. Yang, A. S. Abyzov, J. W. P. Schmelzer, J. Rodríguez-Viejo, Q. Zhai, C. Schick, and Y. Gao, Nano Lett. **17**, 7751 (2017).
39 J. E. K. Schawe, and J. F. Löffler, Nat. Commun. **10**, 1337 (2019).
40 Y. Xie, S. Sohn, M. Wang, H. Xin, Y. Jung, M. D. Shattuck, C. S. O'Hern, J. Schroers, and J. J. Cha, Nat. Commun. **10**, 915 (2019).
41 L. J. Song, M. Gao, W. Xu, J. T. Huo, J. Q. Wang, R. W. Li, W. H. Wang, and J. H. Perepezko, Acta Mater. **185**, 38 (2020).
42 J. Burke, *The Kinetics of Phase Transformations in Metals* (Pergamon, Oxford, 1965).
43 S. Ranganathan, and M. Von Heimendahl, J. Mater. Sci. **16**, 2401 (1981).
44 J. W. Christian, *The Theory of Transformations in Metals and Alloys* (Pergamon, Oxford, 2002).
45 M. Ohta, and Y. Yoshizawa, Mater. Trans. **48**, 2378 (2007).